Assessing sulfur redox state and distribution in abyssal serpentinites using XANES spectroscopy

Baptiste Debret, Muriel Andreani, Adélie Delacour, Stéphane Rouméjon, Nicolas Trcera, Helen Williams

Earth and Planetary Science Letters 466 (2017) 1–11

Contents lists available at ScienceDirect

Earth and Planetary Science Letters

www.elsevier.com/locate/epsl

Assessing sulfur redox state and distribution in abyssal serpentinites using XANES spectroscopy

Baptiste Debret [a,*], Muriel Andreani [b], Adélie Delacour [c], Stéphane Rouméjon [d], Nicolas Trcera [e], EIMF (Edinburgh Ion Microprobe Facility) [f], Helen Williams [a]

[a] Department of Earth Sciences, University of Cambridge, Downing Street, Cambridge CB2 3EQ, UK
[b] Laboratoire de Géologie de Lyon, UMR5276, ENS — Université Lyon 1, Villeurbanne, France
[c] Univ. Lyon, UJM-Saint-Etienne, Laboratoire Magmas et Volcans, UMR 6524, F-42023 Saint-Etienne, France
[d] Department of Earth Sciences, Institute of Geochemistry & Petrology, ETH Zürich, Switzerland
[e] Synchrotron SOLEIL, l'Orme des merisiers, St Aubin BP48, 91192 Gif-sur-Yvette Cedex, France
[f] School of Geosciences, University of Edinburgh, Edinburgh EH9 3JW, UK

ARTICLE INFO

Article history:
Received 21 September 2016
Received in revised form 16 February 2017
Accepted 17 February 2017
Available online 16 March 2017
Editor: T.A. Mather

Keywords:
sulfur sequestration
sulfate
sulfide
micro-XANES
serpentinite
mid-oceanic ridge

ABSTRACT

Sulfur is one of the main redox sensitive and volatile elements involved in chemical transfers between earth surface and the deep mantle. At mid-oceanic ridges, sulfur cycle is highly influenced by serpentinite formation which acts as a sink of sulfur under various oxidation states (S^{2-}, S^{-}, S^{0} and S^{6+}). Sulfur sequestration in serpentinites is usually attributed to the crystallization of secondary minerals, such as sulfides (e.g. pyrite, pyrrhotite) or sulfates (e.g. anhydrite). However, the role of serpentine minerals as potential sulfur carriers is not constrained. We investigate the distribution and redox state of sulfur at micro-scale combining in situ spectroscopic (X-ray absorption near-edge structure: XANES) and geochemical (SIMS) measurements in abyssal serpentinites from the SWIR (South West Indian Ridge), the Rainbow and the MARK (Mid-Atlantic Ridge, Kane Fracture Zone) areas. These serpentinites are formed in different tectono-metamorphic settings and provide a meaningful database to understand the fate of sulfur during seafloor serpentinization. XANES spectra of serpentinite powders show that the sulfur budget of the studied samples is dominated by oxidized sulfur ($S^{6+}/\sum S = 0.6–1$) although sulfate microphases, such as barite and anhydrite, are absent. Indeed, μ-XANES analyses of mesh, bastite and antigorite veins in thin sections and of serpentine grains rather suggest the presence of S^{6+} ions incorporated into serpentine minerals. The structural incorporation of S in serpentine minerals is also supported by X-ray fluorescence mapping revealing large areas (1600 μm^2) of serpentinite where S is homogeneously distributed. Our observations show that serpentine minerals can incorporate high S concentrations, from 140 to 1350 ppm, and that this can account for 60 to 100% of the sulfur budget of abyssal serpentinites. Serpentine minerals thus play an important role in S exchanges between the hydrosphere and the mantle at mid-oceanic ridges and may participate to S recycling in subduction zones.

1. Introduction

Sulfur is a redox sensitive and fluid mobile element that is extensively involved in chemical exchange between the Earth's surface and deep interior. Sulfur is likely to have played an important role in the redox evolution of Earth through geological times (e.g. Canfield, 2005) given that: (1) S can be hosted by either minerals or fluids within a large range of valence states (from S^{2-} to S^{6+}) and thus be an agent of fluid redox exchanges between Earth reservoirs; and (2) even in relatively small concentrations, it can carry significant redox budget, because eight electrons are necessary to oxidize sulfur from S^{2-} in sulfide to S^{6+} in sulfate. The global S cycle is highly influenced by serpentinites (e.g. Alt et al., 2013; Evans, 2012) which are a ubiquitous lithology of the oceanic lithosphere generated at slow and ultra-slow spreading ridges (Andreani et al., 2007; Canales et al., 2000; Sauter et al., 2013), and within subduction zones, as a part of the subducting slab, slab/wedge interface and/or the mantle wedge (Debret et al., 2013; Hattori and Guillot, 2007; Reynard, 2013). Serpentinite formation is a major sink of sulfur during lithosphere hydration at mid-oceanic ridges (e.g. Alt et al., 2013; Alt and Shanks, 2003; Delacour et al., 2008a, 2008b; Schwarzenbach et al., 2012) and serpentinites are a source of sulfur-rich fluids for the mantle wedge

* Corresponding author.
E-mail address: ba.debret@gmail.com (B. Debret).

http://dx.doi.org/10.1016/j.epsl.2017.02.029

during slab dehydration in subduction zones (e.g. Alt et al., 2012; Debret et al., 2014a; Debret et al., 2016; Evans, 2012). A number of studies have documented variations in sulfur concentrations and isotope compositions in bulk rock serpentinites in various environments (e.g. Alt et al., 2007, 2013; Alt and Shanks, 1998, 2003; Delacour et al., 2008a, 2008b; Schwarzenbach et al., 2012). Here we complement these observations by providing new data on sulfur distribution and redox state in serpentine minerals.

At mid-oceanic ridges, serpentinization produces significant amounts of H_2 and CH_4 in response to iron oxidation (e.g. Andreani et al., 2013; Berndt et al., 1996; Charlou et al., 2002; Klein and Bach, 2009; Cannat et al., 2010):

$$2FeO + H_2O_{(aq)} = Fe_2O_3 + H_{2(aq)} \quad (1)$$

The first stages of serpentinization are associated with the desulfurization of mantle peridotite (Frost, 1985). In contrast, the drop of reducing capacity of the peridotite and H_2 activities through the serpentinization process allow the precipitation of hydrothermal sulfides such as pyrite, pyrrhotite, chalcopyrite, pentlandite, heazlewoodite or millerite (Klein and Bach, 2009):

$$S_2 + 2H_{2(aq)} = 2H_2S_{(aq)} \quad (2)$$

$$Fe_3O_4 + 6H_2S_{(aq)} = 2H_{2(aq)} + 4H_2O_{(aq)} + 3FeS_2 \quad (3)$$

Over the last twenty years, extensive sulfur isotope measurements and the chemical extractions of sulfides and sulfates from serpentinites have revealed the widespread existence of sulfate-rich serpentinites in several oceanic and ophiolitic settings (Alt et al., 2013; Alt and Shanks, 1998, 2003; Delacour et al., 2008a, 2008b; Schwarzenbach et al., 2012). The amount and redox state of sulfur stored in serpentinites broadly depends on the conditions under which serpentinization takes place. For example, in high-temperature (>300 °C) systems, abyssal serpentinites display high sulfur concentrations (~2000 ppm, up to >1 wt%) and a high modal abundance of sulfides (Alt et al., 2013; Alt and Shanks, 2003). In these settings, the precipitation of sulfides is generally attributed to the percolation of high-temperature (>300 °C) S-bearing fluids that previously leached sulfides from the adjacent metagabbros (Alt and Shanks, 2003). In contrast, serpentinites formed through the interaction seawater at temperature ranging from 200 to 300 °C and at high water/rock ratio (e.g. exposure near the seafloor) display relatively low amounts of sulfur (~300–1000 ppm), predominantly as sulfate (Alt et al., 2013; Delacour et al., 2008a, 2008b; Schwarzenbach et al., 2012). The whole-rock $\delta^{34}S$ values of sulfate-rich serpentinites typically range from 20‰ (seawater values) to 5‰, suggesting a mixture of seawater sulfate and sulfate derived from oxidation of lower $\delta^{34}S$ mantle sulfides (Alt and Shanks, 2003; Delacour et al., 2008a). In these bulk rock studies, the sulfate budget is usually considered to be the result of the crystallization of sulfate-rich phases, such as barite or anhydrite (e.g. Alt and Shanks, 2003). However, the absence of these phases in sulfate rich serpentinites (e.g. Alt and Shanks, 2003; Delacour et al., 2008a) questions the process of sulfur sequestration and partitioning between serpentine minerals, sulfides and fluids during peridotite alteration.

Recent in situ S concentration analyses of serpentine minerals show that serpentine textures, such as mesh and bastite, can display variable sulfur concentrations ranging from 100 to 1000 ppm (Debret et al., 2014a; Orberger et al., 1999), suggesting that sulfur may be present as nano-phases (e.g. pyrite, pyrrhotite, anhydrite) or incorporated as ions (e.g. S^{2-}, SO_3^{2-}, SO_4^{2-}) in the serpentine structure. Indication in support of direct sulfur incorporation in serpentine minerals includes a positive correlation between F and S during the serpentinization process (Debret et al., 2014a), as sulfur bearing minerals (e.g. pyrite, pyrrhotite, anhydrite) are fluorine free. Experimental and natural studies have also suggested that serpentine minerals can trap various chemical elements and/or nanophases (Brearley et al., 2007; Mellini, 2005; Pabst et al., 2011; Wunder et al., 2010). Lizardite and chrysotile, the two main serpentine varieties identified in abyssal serpentinites, display two different structures as a response to the geometrical misfit of their 1:1 layers composed of octahedral $[Mg_3O_2(OH)_4]^{2-}$ and tetrahedral $[Si_2O_5]^{2-}$ sheets. Lizardite has a flat-layered structure and the misfit is accommodated by the incorporation of smaller ions, e.g., Al^{3+} for Mg^{2+} [6], or larger ions, e.g., Al^{3+} and Fe^{3+} for Si^{4+} [4]. The chrysotile structure is roll-layered and forms open tubes, where the tetrahedral component is on the inside of the rolled-up sheet. Both structures have been proposed as potential traps for elemental clusters during the serpentinization (e.g. Brearley et al., 2007; Pabst et al., 2011; Wunder et al., 2010). However, no direct evidence of sulfur sequestration and its redox state in serpentine minerals was available at that time.

X-ray absorption near-edge structure (XANES) spectroscopy is a powerful tool to identify the oxidation state of sulfur and its atomic environment in mineral structures (e.g. Fleet, 2005; Wilke et al., 2011). Recent studies have used this tool to identify the presence of micro-phases and/or the structural incorporation of various elements (e.g. As, Sb, Cs or Fe^{3+}) in serpentine minerals (Andreani et al., 2013; Debret et al., 2014b; Hattori et al., 2005; Lafay et al., 2016). In this study, we employ XANES spectroscopy, X-ray chemical mapping and SIMS analyses to track the fate of sulfur during the serpentinization of abyssal peridotites. In order to give an overview of sulfur sequestration in serpentine textures formed in different environments, we have studied a set of dredged or drilled samples from (1) the easternmost Southwest Indian Ridge (SWIR, 62°–65°E), (2) the Rainbow massif (36°N) and (3) the Kane transform fault area (23°N) along the Mid-Atlantic Ridge (MARK). We show that serpentine minerals can store S^{6+} ions in their structure and thus may actively participate in global sulfur cycles. Our results reveal that the amount of sulfur incorporated by serpentine minerals varies according to geological setting: in pervasive and seawater-dominated systems serpentine minerals display relatively high sulfur contents and mantle sulfides are consumed during peridotite serpentinization. The crystallization of hydrothermal sulfides in serpentinites seems to be restricted to peridotite/metagabbros fluid interactions at depth or near to hydrothermal fields and leads to a decrease of sulfur content in serpentine minerals.

2. Sample selection

Our study is based on serpentinized peridotites exhumed along detachment faults at slow and ultra-slow spreading ridges. Our sample sites include: (1) the easternmost SWIR, between 62° and 65°E, where mantle peridotites are exhumed on the seafloor along large-offset detachment faults and are associated with minor amounts of basalts and gabbros (<3%) (Sauter et al., 2013). This nearly amagmatic system is considered as an end-member case of serpentinization in which the composition and temperature of the serpentinizing fluids are not influenced by prior interactions with magmatic rocks (Rouméjon et al., 2015). Serpentinization temperatures, derived from oxygen isotope values, range from 270 °C to 340 °C and fluid compositions are mostly controlled by the ultramafic protolith and are close to that of seawater (Rouméjon et al., 2015); (2) the Rainbow hydrothermal field, located on the western flank of the Rainbow massif at 36°14′N along the MAR. The Rainbow massif is composed of serpentinized peridotites associated with significant gabbros and a sediment cover. The dominant hydrothermal alteration of the massif basement is an early widespread and pervasive circulation of seawater-derived fluids associated with serpentinization temperatures ranging from 160

to 260 °C (Andreani et al., 2014). Near the venting area (stockwork), the circulation of high temperature (~360 °C) and acidic (pH ~3.5) fluids enhances serpentinite recrystallization and sulfide precipitation (Andreani et al., 2014; Charlou et al., 2002; Marques et al., 2007). The Rainbow vent fluids are characterized by the highest S and metal (Fe, Mn, Cu, Zn and Co) concentrations ever reported for MAR hydrothermal vents in mafic and ultramafic environments (Charlou et al., 2002). Such off-axis hydrothermal circulations are fueled by large magmatic body at depth (Marques et al., 2007); (3) the MARK area, located along a scarp bounding the MAR at 23°21N, 30 km south of its intersection with the Kane transform fault. This massif is composed of serpentinites and gabbros recording extensive fluid/rock interaction. The serpentinites exhibit multiple stages of serpentinization that is presumed to have taken place at high temperatures (from 250 to 350 °C) involving fluids that previously interacted with metagabbros (Agrinier and Cannat, 1997; Andreani et al., 2007; Alt and Shanks, 2003). No low temperature seafloor weathering minerals (e.g. carbonate, hematite, hydroxides) were observed in the studied samples. In addition, the oxygen isotopes values of the studied samples suggest temperatures of serpentinization ranging from 160 to 350 °C which are not compatible with seafloor weathering.

3. Methods

3.1. X-ray absorption spectroscopy

The X-ray absorption near edge structure (XANES) spectra at S K-edge were collected at the LUCIA beamline (SOLEIL synchrotron, France). Si(111) double-crystal monochromators were used. Measurements were collected with the following configuration for the storage ring: current of 400 mA and energy of 2.75 GeV. All XANES spectra were measured in fluorescence mode using a four-element silicon drift diode (SDD) detector. The beam spot was unfocalized for the analysis of standards and powdered samples and was set to 3×3 μm^2 size using two dynamically bendable mirrors in a Kirkpatrick–Baez configuration for serpentine grains and thin sections analyses. XANES spectra were acquired from 2420 to 2540 eV. We used a sampling step of 2 eV between 2420 and 2464 eV, 0.5 eV from 2464.5 to 2490 eV, 1 eV between 2491 and 2540 eV. To improve signal-to-noise ratio, each XANES spectrum is the average of 4 spectra acquired at the same point. X-ray fluorescence (XRF) chemical maps were used to constraint the distribution of sulfur at the micro-scale, identify sulfur-bearing minerals (e.g. sulfides; see Appendix A) in the thin sections and select spots for XANES measurements. The XRF chemical maps were acquired with a step of 4 or 5 µm and an energy of 2550 eV. XANES spectra were normalized using the Athena© software (Ravel and Newville, 2005).

It is known that the S K-edge position varies with S oxidation state (e.g. Klimm et al., 2012). This method is an extremely powerful technique that is widely applicable to the problem of speciation of S in silicate melts, glasses, S-rich minerals and silicates (e.g. Alonso Mori et al., 2009; Fleet, 2005; Jugo et al., 2010; Métrich et al., 2002). However, under some experimental conditions beam-related damage has been reported, and some earlier results have been discredited (Métrich et al., 2009; Wilke et al., 2008). In order to avoid any analytical artefacts related to changes in the sulfur species caused by irradiation with the beam, we (1) compared serpentinite spectra taken with an unfocused and a focused beam, and (2) monitored beam irradiation effects during 120 min by acquiring 110 spectra with a focused beam and a short acquisition time of ~1 min. No changes for XANES spectra depending on photo-oxidation/reduction effects (e.g. Wilke et al., 2008) were observed (see Appendix B). We tested the reproducibility of serpentinite spectra taken with an unfocused beam by measuring four sets of the same powdered sample and did not observe any modification of the spectra produced (Appendix B). During the in situ analyses of thin sections, the presence of epoxy resin associated with serpentine textures was easily identified by three additional peaks at 2468, 2472 and 2476 eV which (Appendix B).

3.2. SIMS analyses

Fluorine, chlorine and sulfur concentrations of serpentine textures were measured using a CAMECA IMS 1270 ion probe at the Edinburgh Ion Microprobe Facility (EIMF), University of Edinburgh. Standard 30-µm-thick sections were cut and pressed into indium filled mounts in order to minimize the number of sample changes during analyses and contribute to better analytical stability (e.g. Debret et al., 2014a; Van den Bleeken and Koga, 2015). BCR-2G international standard basalt glasses were also inserted into every mount and used as monitor for detecting machine drift. Each mount was gold coated prior to analyses. Every spot was presputtered for 150 s with 15-µm rastered beam, then spots were analyzed with a <5 µm beam (determined by image field), using a Cs^+ primary beam and a primary accelerating voltage of 10 kV. ^{28}Si, ^{18}O, ^{19}F, ^{35}Cl and ^{32}S measurements were obtained at a mass resolution of 3,500, an energy window of 60 eV and a single electron multiplier detector using magnetic peak switching. Each analysis consists of 20 cycles. ^{28}Si and ^{18}O were counted for 2 s each and ^{19}F, ^{35}Cl and ^{32}S for 4 s each. The intensity measured at masses ^{19}F, ^{35}Cl and ^{32}S were normalized to ^{18}O. The F, Cl and S contents were determined using relative ion yield in BCR-2G. The accuracy of this method has been tested by repeated measurements of international and laboratory glass standards (Fba-1, 2, 3, 4, 5, ATHO, T1G, KL2, L17, MD57) as well as mineral standards (AL96-10, Vol. 4; see Appendix C for preferred values and Van den Bleeken and Koga, 2015 for matrix issues and long term reproducibility). The position of the incident beam on the samples was checked based on optical microscopy and Raman spectroscopy after the SIMS sessions to ensure correct mineral phases were analyzed. Although the beam size used during SIMS analyses was relatively small (~5 µm), all serpentine minerals have a smaller grain size (<0.5 µm), such that each analysis corresponds to a mixture of several grains of serpentine and in some case of accessory phases (e.g. sulfides) associated with serpentine crystals. Volatiles concentrations are given in Appendix D.

4. Results

4.1. Sulfur distribution in serpentinites

Two samples per area were selected for this study. Those samples are considered to be representative of the different stages of serpentinization affecting each area. (1) The SWIR samples correspond to extensively (~100%) serpentinized harzburgites dredged during the Smoothseafloor cruise (SMS_DR2-2-8 and SMS_DR5-3-26a). They display mesh and bastite textures replacing olivine and orthopyroxene, respectively (Fig. 1a). Those textures are comprised of lizardite and chrysotile mixtures (Rouméjon et al., 2015). Sample SMS_DR5-3-26a contains late antigorite veins crossing mesh and bastite textures and is composed of disoriented and elongated blades of less than 10 µm long. In these textures, sulfur is homogeneously distributed (Fig. 1a) and no accessory sulfur-rich phases (sulfide or sulfate) were observed at micro- or nano-scale (see Rouméjon et al., 2015 for nano-scale observations of the studied samples). (2) The Rainbow samples were dredged during the MoMARDREAM 2008 cruise (Andreani et al., 2014). They correspond to one serpentinite from the massif basement (DR08_07a) and one mineralized serpentinite located close to

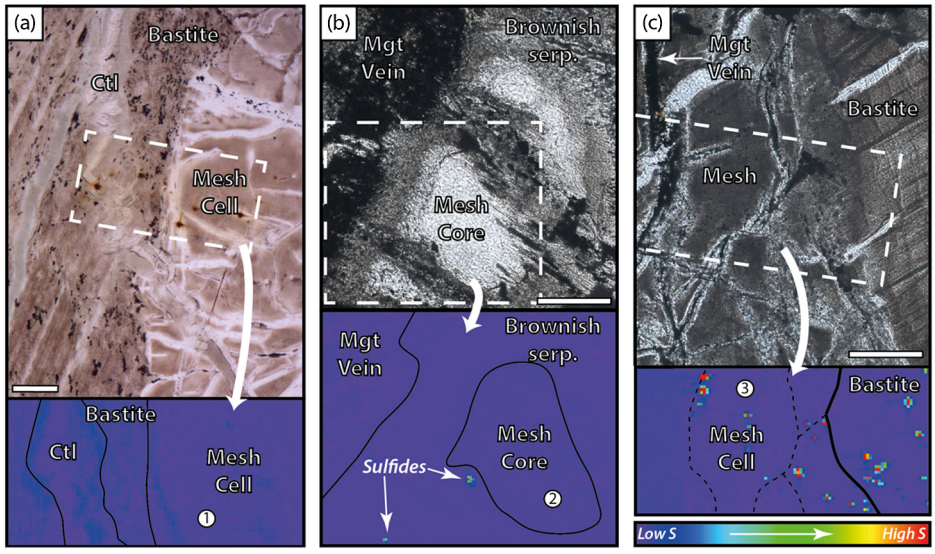

Fig. 1. Microphotographs and XRF chemical maps at 2550 eV of serpentinites formed at (a) the SWIR (SMS_DR2-2-8), (b) the Rainbow stock work (DR12_01a) and (c) the MARK area (L7). The white bar is 100 µm. (a) Mesh and bastite textures crossed by a late chrysotile vein (Ctl). The S is homogeneously distributed in the sample without any S-rich accessory phases. (b) Mineralized mesh texture displaying a fresh, non-mineralized, core partly recrystallized into brownish serpentine. The brownish texture is associated with micro-sulfides (mainly pyrrhotite). (c) Contact between mesh and bastite textures. These textures are associated with various micro-sulfide grains (mainly pyrite and pyrrhotite). On the XRF chemical map, the contact between bastite and meshes is marked by a bold line. Mesh cells are divided by dashed lines. The colors of the XRF maps correspond to sulfur concentrations. Nos. 1, 2, 3: beam location of XANES analyses in low sulfur concentration area, the corresponding spectra are displayed in Fig. 4. (For interpretation of the references to color in this figure legend, the reader is referred to the web version of this article.)

the active hydrothermal vents (DR12_01a). Sample DR08_07a is a highly serpentinized peridotite (>80%) displaying mesh and bastite textures. The DR12_01a displays mesh and bastite textures that have been partly to fully replaced by brownish serpentine (Fig. 1b). The XRF chemical mapping of the mesh and bastite textures of the Rainbow serpentinites reveals large serpentine areas with homogeneous S concentrations (Fig. 1b). The Rainbow DR12_01a sample contains additional sulfides of about 10 µm, mainly pyrrhotite, disseminated into mineralized textures (Fig. 1b). (3) The studied MARK serpentinites correspond to highly serpentinized peridotites (>80%) drilled at the ODP Holes 920 B and D during Leg 153 (153-920D-14R2pc4 and 153-920B-3R1pc5, named L10 and L7 respectively in the rest of the manuscript). Both samples display common mesh and bastite textures (Fig. 1c). XRF chemical mapping of the mesh and bastite textures of MARK serpentinites show that sulfur is carried by serpentine and sulfides. The mesh and bastite textures are composed of serpentine associated with micro-inclusions of about 5–10 µm corresponding mainly to pyrrhotite and pyrite. The relative proportion of micro-sulfides appears to increase toward the bastite textures (Fig. 1c).

4.2. Bulk rock and micro-XANES analyses of serpentinites

Serpentinites are polyphase rocks composed of silicate minerals (mainly serpentine, olivine and orthopyroxene) and magnetite that can be associated with various metal alloys (e.g. awaruite) and sulfide species (e.g. Klein and Bach, 2009). In order to constrain the fate of sulfur during serpentinization, we analyzed a set of model S-rich compounds that were used as references and compared to serpentinite and serpentine minerals spectra. Fig. 2 shows a compilation of the analyzed sulfide (S^{2-} and/or S^{-}), sulfur (S^{0}), synthetic sulfite (S^{4+}) and sulfate (S^{6+}) standards. Each spectrum is characterized by an intense edge followed by a broad shoulder. The position of the S-edge and its intensity are related to the binding energies of the valence orbitals and mainly depend on sulfur oxidation state (Fleet, 2005; Wilke et al., 2011; Table 1). The post edge shoulder pattern is modulated by the nature of the bonding between sulfur and the neighboring atoms, and by the chemical composition of the considered crystal (Fleet, 2005). Hence, the absorption spectrum near the edge is modulated by the oxidation state and the nearest-neighbor elements of sulfur providing enough information to discuss sulfur incorporation at small scale.

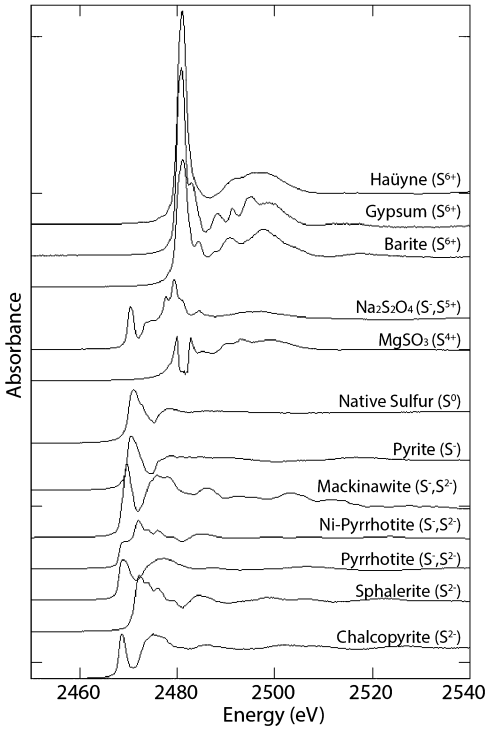

Fig. 2. Normalized S K-edge XANES spectra of powdered sulfides, native sulfur, sulfites and sulfates. Spectra are background-subtracted and normalized to edge-jump. S^{2-}: chalcopyrite ($CuFeS_2$), sphalerite ([Zn,Fe]S); S^{-}/S^{2-}: pyrrhotite ($Fe_{1-X}S$, X = 0–0.2), Ni-pyrrhotite ($[Fe,Ni]_{1-X}S$, X = 0–0.2), mackinawite ($[Fe,Ni]_{1+X}S$, X = 0–0.11); S^{-}: pyrite (FeS_2); S^{0}: native sulfur (S); S^{4+}: Na_2SO_3 and $MgSO_3$; S^{6+}: barite ($BaSO_4$), gypsum ($CaSO_4 2H_2O$), Haüyne ($[Na,Ca]_{4-8}[Al_6Si_6(O,S)_{24}][SO_4,Cl]_{1-2}$).

Table 1
Main XAS features of standard.

Standard name	Formula	Edge (eV)	Main shoulders (eV)
Chalcopyrite	$CuFeS_2$	2469	2475, 2486, 2502, 2509
Sphalerite	[Zn, Fe]S	2472[a], 2474, 2476, 2479	2484.5, 2493, 2499, 2506
Pyrrhotite	$Fe_{1-X}S$	2469	2477, 2487.5, 2507
Ni-Pyrrhotite	$[Fe, Ni]_{1-X}S$	2469, 2472[a], 2476, 2479	2484.5, 2499, 2507
Mackinawite	$[Fe, Ni]_{1+X}S$	2470	2477, 2486, 2494, 2503.5, 2512, 2514
Pyrite	FeS_2	2471	2485.5, 2506, 2517
Native sulfur	S	2471	2478, 2486.5
Thiosulfate	$Na_2S_2O_3$	2470.5, 2477, 2479	2474, 2484, 2496
$MgSO_3$		2480, 2483	2486, 2490, 2493.5, 2499.5
Barite	$BaSO_4$	2481	2484, 2491, 2497.5
Gypsum	$CaSO_4 2H_2O$	2481	2483, 2488, 2491, 2495, 2499
Haüyne	$[Na, Ca]_{4-8}[Al_6Si_6(O,S)_{24}][SO_4, Cl]_{1-2}$	2481	2491, 2497

[a] Main peak.

Table 2
Main S-bearing phases and XAS features of the samples.

Sample name	Locality	S-bearing phases	Edges	Main shoulders	S^{6+}/S_{Tot}
3651-1252	Atlantis	serp.	(2472) 2481	2490, 2497	1 *(0.98)*
SMS_DR228	SWIR	serp.	2481	2497	1
DR08_07a	Rainbow	serp./pyrrhotite/pyrite	2469, 2471, 2481	2497	0.85
DR12_01a	Rainbow	serp./pyrrhotite +/−pyrite	2469, 2481	2475, 2497	0.55
L7	MARK	serp./ pyrrhotite	2469, 2481	2475, 2497	0.65
L10	MARK	serp./ pyrrhotite	2469, 2481	2475, 2497	0.75
H03-R2301	Atlantis	serp./ pyrite	2471, 2481	2485, 2495	0.15 *(0.14)*

(Regular): small feature; *(italic)*: chemical separation estimates (Delacour et al., 2008a, 2008b).

The edge position of Fe-bearing sulfides (chalcopyrite, pyrrhotite, mackinawite and pyrite) is comprised between 2469 and 2471 eV followed by a broad shoulder between 2475 and 2480 eV (Fig. 2, Table 1). As noted in previous studies, the incorporation of Ni or Zn (Ni-pyrrhotite and sphalerite) is accompanied with a disappearance of the prominent peak at 2469–2471 eV and considerable oscillations on the edge shape (Alonso Mori et al., 2009; Fleet, 2005; Wilke et al., 2011). The edges of the S^{4+} and S^{5+} in synthetic sulfites are present between 2479 and 2480 eV (Fig. 2). The XANES spectrum of the $Na_2S_2O_3$ synthetic thiosulfate is composed of two edges at 2470.5 eV and 2479 eV corresponding to S^- and S^{5+} respectively. In the sulfites $Na_2S_2O_3$ and $MgSO_3$ variable chemical compositions generate different atomic environments for sulfur, which have a strong influence on the XANES (see also Alonso Mori et al., 2009; Wilke et al., 2011). The highest energy position of the edge is found for sulfates (barite, gypsum and haüyne) which all display a very strong peak at 2481 eV (Fig. 2). Sulfate shoulders at higher energies vary in intensity and position among the different sulfates according to the S-structural environment. The anhydrous sulfate (barite) spectrum displays three different shoulders at 2484, 2490 and 2497 eV while hydrous sulfate (gypsum) has four shoulders at 2483, 2488, 2491 and 2495 eV and a broad feature around 2500 eV. Haüyne is a sodalite group mineral in which structures cavities are occupied by SO_4^{2-} (and/or Cl^-) ions usually coordinated by Ca and Na ions. Its spectrum is characterized by a broad feature between 2486 and 2505 eV and a small shoulder at 2491 eV.

The XANES spectra of the serpentinite powders are shown in Fig. 3. We tested the accuracy of XANES analyses by measuring two powdered serpentinites of known $S^{6+}/\sum S$ (determined by chemical extraction of the sulfate and sulfide fractions, see Delacour et al., 2008a, 2008b), from the Atlantis massif, with contrasted $S^{6+}/\sum S$ ratios of 0.14 (H03-R2301) and 0.98 (3651-1252). In agreement with the chemical analyses, the two samples from Atlantis massif display highly contrasted XANES spectra (Fig. 3). The H03-R2301 sample spectrum has two intense peaks at 2471 eV and 2481 eV corresponding respectively to pyrite and oxidized sulfur (S^{6+}) and a broad shoulder between 2485 and 2500 eV. The

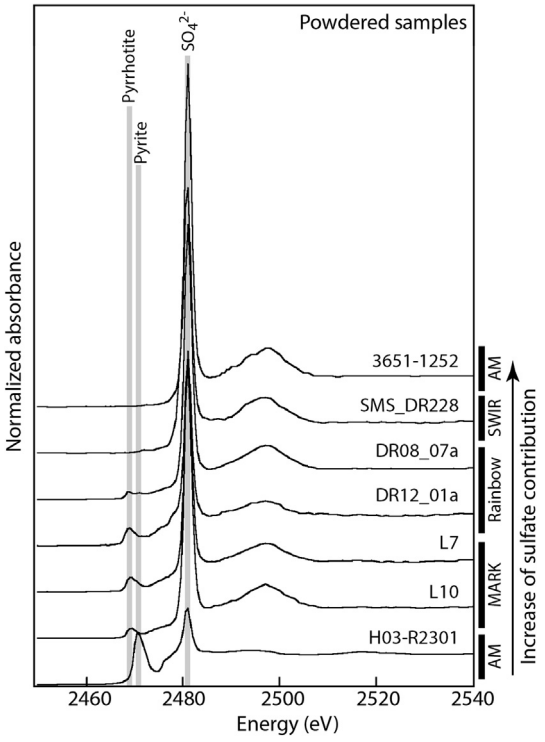

Fig. 3. Normalized S K-edge XANES spectra of powdered serpentinites. Spectra are background-subtracted and normalized to edge-jump. Atlantis Massif (AM): 3651-1252 and H03-R2301; MARK: L7 and L10; Rainbow: DR08_07a and DR12_01a; SWIR: SMS_DR228. The S budget of the SWIR sample is exclusively carried by oxidized sulfur (S^{6+}) while that of Rainbow and MARK samples are carried by oxidized (S^{6+}) and reduced (pyrite and pyrrhotite) sulfur.

3651-1252 sample spectrum is dominated by an intense peak at 2481 eV and a broad shoulder between 2485 and 2500 eV corresponding to oxidized sulfur (S^{6+}). XANES analyses were also performed on one powdered sample from the SWIR (SMS_DR228) and two powdered samples from the Rainbow (DR08_07a and

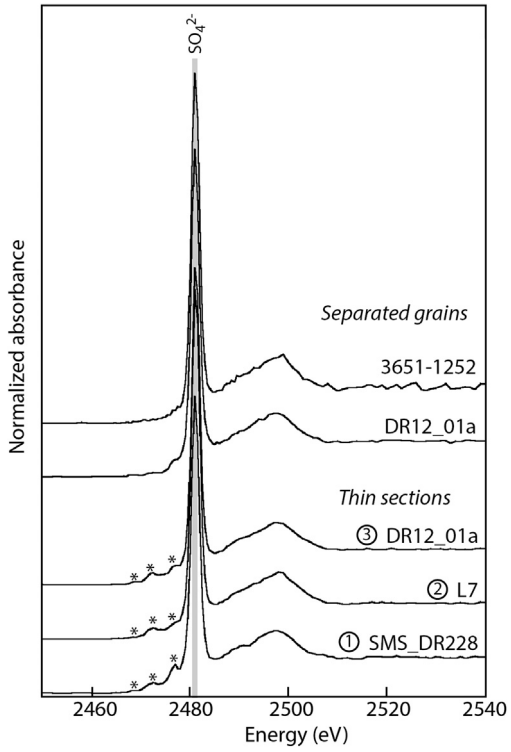

Fig. 4. Normalized S K-edge XANES spectra of serpentine minerals (in situ analyses of serpentine grains and serpentine textures in thin section analyses). The thin section analyses (see Fig. 1 for analyses location) show additional peaks (marked by ∗) corresponding to epoxy.

DR12_01a) and MARK (L7 and L10) areas (Table 2, Fig. 3). The XANES spectrum of the SWIR sample is dominated by oxidized sulfur (S^{6+}) while the spectra of Rainbow and MARK samples corresponds to a mixture between oxidized (S^{6+}) and reduced (pyrite and pyrrhotite) sulfur (Fig. 3). The Rainbow samples display contrasting XANES spectra. Sample DR08_07a display a strong oxidized sulfur peak at 2481 eV and two discrete peaks at 2469 and 2471 eV corresponding to pyrrhotite and pyrite, respectively. In comparison, sample DR12_01a displays a marked peak at 2469 eV corresponding to pyrrhotite. This shows a relative increase in sulfide amounts in serpentinites formed near the hydrothermal vents.

In addition to serpentinite powder analyses, spot µ-XANES analyses of serpentine grains and mesh or bastite textures in thin sections were also carried out. The µ-XANES analyses of separated grains of serpentine are characterized by a very strong peak at 2481 eV and broad features between 2485 and 2500 eV (Fig. 4). Such observations are similar to those made during the analyses of haüyne (Fig. 1; see also Fleet, 2005; Wilke et al., 2011). Three sections were also selected for µ-XANES analyses (samples SMS_DR2-2-8, DR12_01a and L7). The µ-XANES spectra of these serpentine areas are similarly dominated by oxidized sulfur (S^{6+}, Fig. 4). Some additional small peaks at 2468, 2472 and 2476 eV are related to epoxy resin (see Appendix B).

4.3. Estimates of $S^{6+}/\sum S$ from XANES spectra

The edge shift between sulfides and sulfates, reaching 12 eV, can be used to estimate the $S^{6+}/\sum S$ of a given material (e.g. Jugo et al., 2010; Wilke et al., 2011). To define the relationship between the relative variation in oxidized and reduced sulfur signals and $S^{6+}/\sum S$ in serpentinites, a sequence of spectra (Fig. 5) was calculated as a series of simple binary mixtures between a S^{6+}-rich serpentine mineral and a reduced sulfide. The measured bulk rock spectra were then compared to calculated spectra to estimate $S^{6+}/\sum S$ ratios, and an example (H2301) is presented in Fig. 5. Most of the measured spectra fall within a calculated $S^{6+}/\sum S$ interval of 0.1 to 0.2 on an energy range between 2460 and 2490 eV (see Fig. 5b). This suggests an uncertainty of about ±0.05 to ±0.1 on $S^{6+}/\sum S$ depending on the presence of multiple sulfide phases, their abundances and the quality of the spectra (e.g. sulfur concentration of the sample). The accuracy of these estimates was also checked with previous chemical extractions of

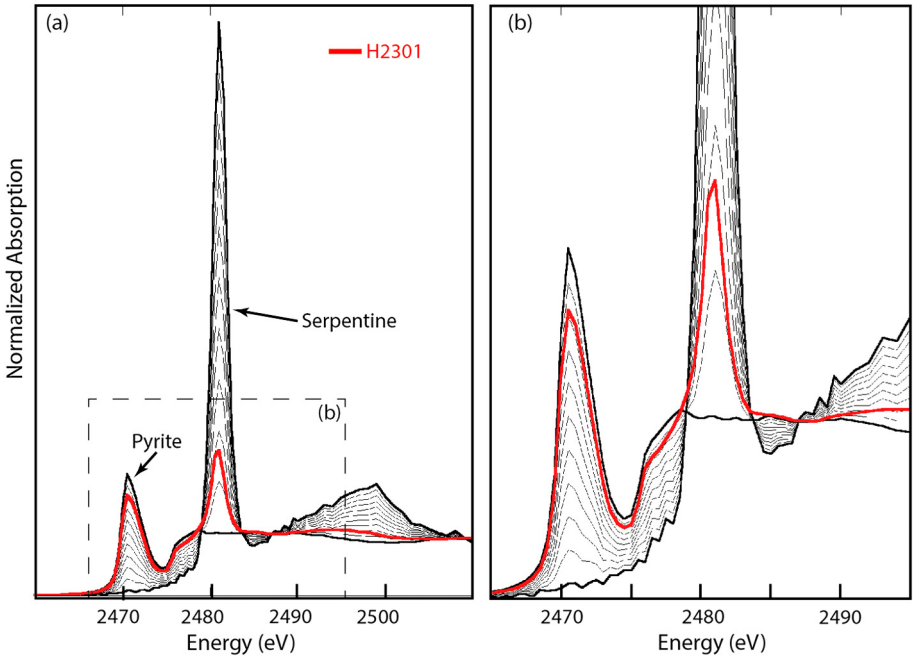

Fig. 5. Estimates of $S^{6+}/\sum S$ from XANES spectra. (a) Spectra of a S^{6+}-bearing serpentine and a pyrite sulfide used as reference for $S^{6+}/\sum S = 1$ and $S^{6+}/\sum S = 0$ (bold spectra), respectively. The thinner spectra are a combination of these two end-members at 0.1 intervals of $S^{6+}/\sum S$. The red spectrum corresponds to that of the H2301 sample. The doted box show the region zoomed in Fig. 5b. The H2301 spectrum is comprised between the intervals 0.1 and 0.2, consistent with bulk rock analyses (see Table 2). (For interpretation of the references to color in this figure legend, the reader is referred to the web version of this article.)

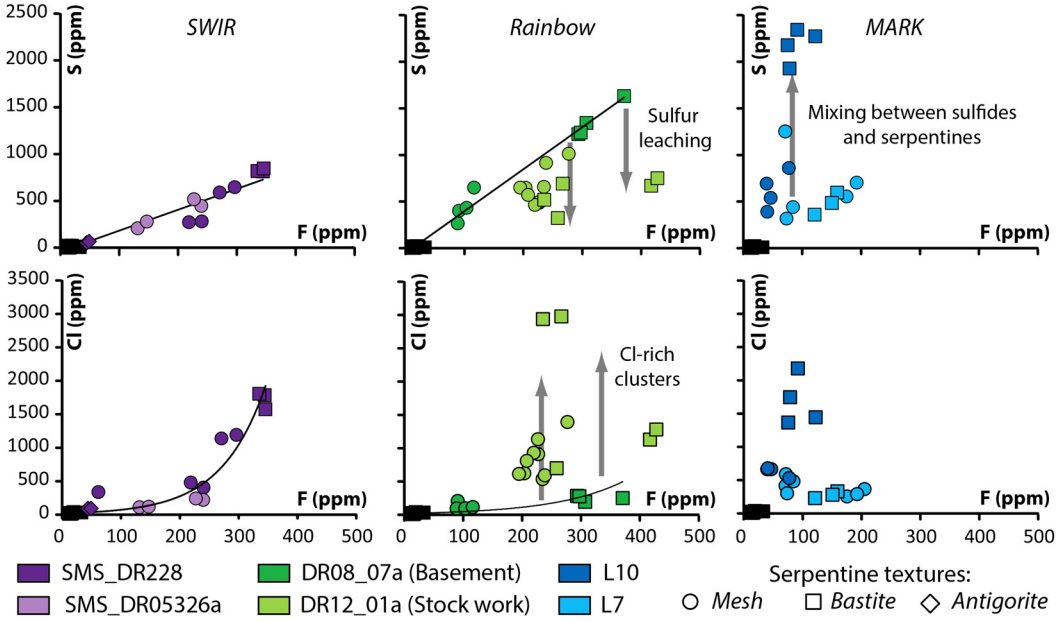

Fig. 6. Plots of S vs F and Cl vs F concentrations in serpentine textures at (a) the SWIR, (b) the Rainbow massif (basement and stock work) and (c) the MARK area.

sulfates and sulfides in Atlantis Massif samples (Delacour et al., 2008a, 2008b). In agreement with chemical extraction data (see Table 2), the $S^{6+}/\sum S$ estimated by XANES is about 0.15 in H2301 sample (Fig. 5b) and close to 1 in 3651-1252. The SWIR sample displays the highest $S^{6+}/\sum S$ ratio (~1). The Rainbow serpentinites have contrasting $S^{6+}/\sum S$ ratios: the mineralized sample has a ratio of ~0.5 while the basement sample is rich in oxidized sulfur ($S^{6+}/\sum S \sim 0.9$). The sulfur budget of MARK serpentinites is carried both by reduced and oxidized sulfur ($S^{6+}/\sum S \sim 0.6$–0.7, which is consistent with Alt and Shanks, 2003 chemical estimate of $S^{6+}/\sum S$ in MARK serpentinites).

4.4. F, Cl and S concentrations of serpentine minerals

Primary minerals display homogeneous F, Cl and S concentrations in the different studied settings. Mantle minerals (olivines and pyroxenes) have low F (11–20 ppm), Cl (8–36 ppm) and S (3–21 ppm) relative to serpentine minerals (Appendix D), which display a wide range of F (17–428 ppm), Cl (91–2977 ppm) and S (53–2342 ppm) concentrations in agreement with previous studies of abyssal serpentinites (Debret et al., 2014a; Orberger et al., 1999). In the SWIR serpentinites, mesh textures have low F (62–296 ppm), Cl (220–1191 ppm) and S (143–646 ppm) concentrations relative to that of bastite textures (F = 335–345 ppm; Cl = 1574–1805 ppm; S = 815–846 ppm). Late antigorite veins are characterized by the lowest F (45–49 ppm), Cl (91–97 ppm) and S (53–61 ppm) concentrations. In the Rainbow serpentinites, F (89–277 ppm) and S (265–1012 ppm) concentrations in mesh and mineralized mesh textures are homogeneous while mineralized brownish meshes are characterized by higher Cl (533–1390 ppm) concentrations (Fig. 6). Bastite textures display heterogeneous Cl (698–2977 ppm) and S (322–1632 ppm) concentrations. The mineralized bastites display high Cl (698–2977 ppm) and low S (322–751 ppm) concentrations relative to bastites (Cl = 192–283 ppm; S = 1224–1632 ppm). In the MARK samples, serpentine textures display heterogeneous and high S (143–2342 ppm) concentrations relative to that of the SWIR or Rainbow areas. The mesh (F = 47–205 ppm, Cl = 290–677 ppm and S = 317–1253 ppm) and bastite (F = 79–159 ppm; Cl = 230–2177 ppm and S = 359–2342 ppm) textures display similar ranges of concentrations.

5. Discussion

5.1. Sulfur sequestration in serpentinites

The XANES spectra of serpentinite powders correspond to mixtures between oxidized (S^{6+}) and reduced (S^{2-} or S^{-}) sulfur which demonstrates the incorporation of both S-species during oceanic serpentinization. Sulfides can be easily recognized in serpentinites by thin sections observations and XRF chemical maps (Fig. 1) and correspond principally to pyrrhotite and pyrite in our samples. In contrast, no sulfate grains were identified at micro or nano-scales in this study or in published works (see Appendix A, Andreani et al., 2007, 2013, 2014 and Rouméjon et al., 2015 for nano-scale observations of the studied samples). This is in good agreement with the XANES spectra of serpentine textures that are similar to those of the sulfate-bearing haüyne suggesting that S is present as S^{6+} within the silicate serpentine minerals (Fig. 4). The exact location of sulfur in serpentine mineral structure remains at that stage speculative. Serpentine minerals can trap sulfur in their structures via various processes and the range of XANES standards for S^{6+}-bearing silicates analyzed here or in the literature are relatively limited. Nevertheless, the strong similarity between XANES spectra of sulfate-bearing haüyne and of serpentine minerals suggest a very similar environment for S in both structure; i.e a tetra-coordinated S. Haüyne is a cubic mineral displaying cage-like cubo-octahedral units, formed by the linkage of SiO_4 and AlO_4 tetrahedra, which are occupied by chloride and/or sulfate ions (Deer et al., 2012, Appendix E). Serpentine minerals are trioctahedral layered silicates that can trap various size ions in their structures (Brearley et al., 2007; Pabst et al., 2011; Wunder et al., 2010) and/or molecules adsorption on their surface (Feuillie et al., 2013). However, the surface adsorption for sulfur cannot explain the similarity between the observed haüyne and serpentine XANES spectra as adsorption occurs mainly on the edges of phyllosilicates by ligand exchange with –OH groups (Feuillie et al., 2013).

Previous studies have also proposed that chrysotile tubes can serve as an important carrier of Li and perhaps of other fluid mobile elements (Wunder et al., 2010). Indeed, the presence of SO_4^{2-} ions into chrysotile tube or haüyne can lead to similar bonding environments in which SO_4^{2-} ions are surrounded by Si and/or Al in

tetrahedral coordination. However, although S concentrations differ between serpentine textures (Fig. 6), it is unlikely that chrysotile nanotubes are the only site for S. Notably, this cannot explain the high and homogeneously distributed S contents of the SWIR and Rainbow serpentine textures (Fig. 1a,b), even if small amounts of nanotube-bound S cannot be precluded at the nano-scale.

An alternative solution is to consider that sulfur could be trapped either via Si substitutions by S in the tetrahedra, or as a sulfate ion in the network of the tetrahedral sheet of serpentine minerals. Indeed the different types of serpentine (e.g. lizardite, chrysotile, antigorite) display pseudo-hexagonal networks of linked SiO_4 tetrahedra (Deer et al., 2012; Appendix E) that can potentially trap ions such as sulfate in their center. This latter configuration would be the closest to haüyne and can could explain the homogeneous and high S concentrations of serpentine textures as well as the similarities between the XANES spectra of haüyne and serpentines.

The addition of S and Cl to serpentine minerals during serpentinization is controlled by serpentinizing fluid composition, serpentine structure and other thermodynamic parameters such as fO_2 and temperature (e.g. Alt et al., 2013; Klein and Bach, 2009). In contrast, F addition is controlled by the local degree of serpentinization and, thus, mostly by the fluid/rock ratio (Debret et al., 2014a). The F concentrations of serpentine can therefore be used as a proxy of serpentinization degree and fluid/rock ratio. The SWIR serpentinites are expected to be formed in equilibrium with a fluid which chemical composition is similar to seawater and thus depleted in S relative to other settings (Rouméjon et al., 2015). During the serpentinization of these rocks, the increase in both S and Cl concentrations is correlated with an increase of serpentine F concentration (Fig. 6a). The precipitation of accessory phases in the serpentinites (e.g. sulfides, sulfates or chlorides) cannot result in the observed positive correlation between F, Cl and S during the serpentinization process because these phases are F-free. Such observations therefore support the hypothesis of a structural incorporation of F, Cl and S into serpentine minerals as serpentinization proceeds. At the Rainbow massif, the serpentinization of the basement is accompanied with a correlated increase in F, Cl and S concentrations suggesting similar conditions of serpentinization (e.g. fluid composition, temperature, fO_2) to that observed at the SWIR. In contrast, in DR12_01a samples, which formed near hydrothermal vents, serpentinites recrystallization is accompanied with a decrease in S and an increase in Cl concentrations in serpentine minerals (Fig. 6b) and the abundant precipitation of pyrrhotite (Fig. 1c and 3).

Element remobilization and sulfide precipitation is a recurrent process observed near hydrothermal events (Andreani et al., 2014; Marques et al., 2007). Sulfur initially present in serpentine is remobilized and reduced into newly formed sulfides as a result of extensive hydrothermal alteration. This process can also be accompanied with the crystallization of Cl-bearing minerals (Marques et al., 2007), explaining the high Cl concentrations in serpentine textures, and the sequestration of chalcophile elements (As, Sb, Pb, Cu, Zn, Co and Ni) in serpentinites (Andreani et al., 2014; Marques et al., 2007). The MARK serpentine textures display high S concentrations relative to that of the Rainbow or SWIR areas (Fig. 6). Several analyses, mostly of bastite textures, are characterized by unusual high S concentrations, reaching up to 2343 ppm (Fig. 6c). These high concentrations are consistent with the presence of micro-sulfides, which can also explain the absence of correlation between F, Cl and S concentrations. For these samples, the XRF chemical maps also reveal the presence of micro-sulfides disseminated within serpentine textures (Fig. 1c).

The crystallization of late antigorite veins in the SWIR serpentinites remains enigmatic as this serpentine variety is mainly observed in subducted settings (e.g. Reynard, 2013). However, Rouméjon et al. (2015) suggested that antigorite crystallization may result from seawater-derived fluid percolation as supported by high B concentrations and negative Ce anomalies obtained from LA-ICP-MS analyses. Nonetheless, antigorite veins display low S concentrations (53–61 ppm) relative to mesh and bastite textures in the SWIR serpentinites (Fig. 6a). These ranges of concentrations are similar to that observed in blueschist and eclogitic ophiolites from the Western Alps (Debret et al., 2014a). It might suggest that antigorite cannot incorporate as much sulfur as lizardite and/or chrysotile in its structure whatever the serpentinizing setting (oceanic ridges or subduction zone). The lizardite/chrysotile to antigorite phase transition that mostly occurs in subduction zones should thus exert a fundamental role on sulfur partitioning between serpentinites and fluids and could potentially lead to sulfur leaching in fluids (Debret et al., 2014a) or its redistribution into newly formed sulfides.

5.2. The fate of sulfur during abyssal peridotite serpentinization

The sulfur budget of mantle peridotites ranges between 60 to 250 ppm depending on peridotite fertility and is exclusively carried by sulfides (Alt and Shanks, 2003). In contrast, serpentinites display a wide range of sulfur concentrations, from 20 ppm to 1 wt%, and sulfur species with various oxidation states (e.g. Alt et al., 2013; Alt and Shanks, 1998, 2003; Delacour et al., 2008a, 2008b) reflecting different processes influencing the sulfur cycle during hydrothermal alteration (Fig. 7).

At the SWIR and Rainbow massif basement, the serpentinization of mantle peridotites occurs as seawater propagates at depth through fractures in the footwall of detachment faults (Rouméjon and Cannat, 2014; Fig. 7a). In this context, XANES spectra of serpentinite powders are dominated by sulfate (Fig. 3). XRF chemical maps of serpentine textures are free of sulfide- (e.g. pyrite, pyrrhotite) or sulfate- (e.g. barite, anhydrite) bearing phases (Fig. 1a) showing that the sulfur budget is exclusively carried by S^{6+}-rich serpentine minerals. Additionally, the absence of mantle sulfides in fully serpentinized peridotites from the SWIR or the Rainbow massif basement suggests that these phases are progressively consumed and oxidized during serpentinization (Figs. 7c,d). This process must be controlled by the local water/rock ratio as seawater can act as a powerful oxidizing agent at mid-oceanic ridges (e.g. Andreani et al., 2013; Berndt et al., 1996; Charlou et al., 2002; Klein and Bach, 2009). In this scenario, the oxidation of mantle sulfides (FeS in Equation (4) for simplicity) to sulfates can also involve the release of H_2-rich fluids, e.g.,

$$2FeS + 11H_2O \rightarrow 2SO_4^{2-} + Fe_2O_3 + 11H_2 \quad (4)$$

Given that fresh mantle fertile peridotites contain up to 250 ppm of reduced sulfur, the oxidation of mantle sulfide during seafloor serpentinization can reduce up to ~0.04 moles of H_2O into H_2 per kilogram of serpentinite. This is, however, a maximum estimate. For example, if sulfur is originally present as mixtures of S^{2-} and S^{-} (e.g. chalcopyrite or pentlandite) then the amount of released H_2 would be significantly lower. Hydrogen (H_2) production at mid-oceanic ridges is usually attributed to the oxidation of Fe^{2+} into Fe^{3+}. Mantle peridotites display low $Fe^{3+}/\sum Fe$ (~0; e.g. Canil et al., 1994) relative to abyssal serpentinites ($Fe^{3+}/\sum Fe$ ~0.7; e.g. Andreani et al., 2013); the mass balance involves the liberation of H_2:

$$2FeO + H_2O = Fe_2O_3 + H_2 \quad (2)$$

Given that abyssal serpentinites contain about ~8 wt% of FeO_{Tot} (e.g. Andreani et al., 2013), the oxidation of iron contribute to reduce ~0.39 moles of H_2O into H_2. Relative to iron oxidation, the oxidation of mantle sulfides can thus account for up to ~10 % of the observed H_2 production at mid-oceanic ridges.

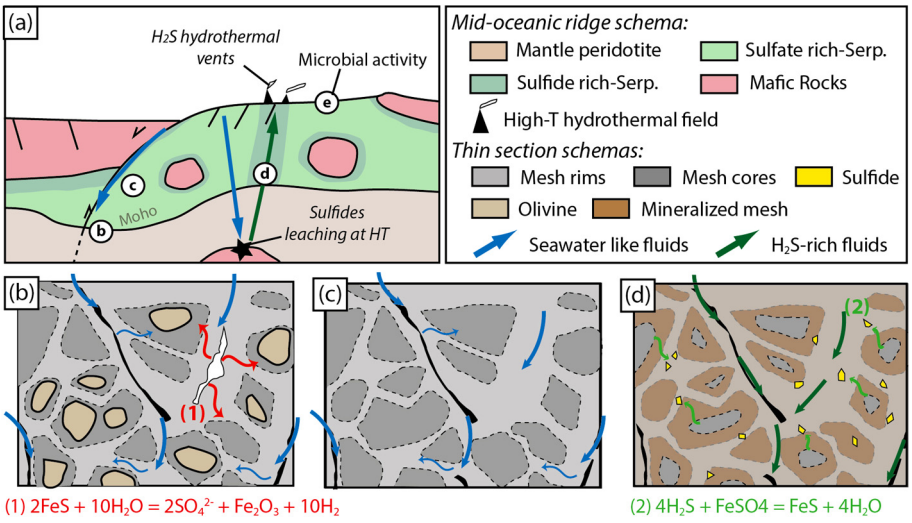

Fig. 7. Conceptual model illustrating the evolution of sulfur distribution and redox state during the serpentinization of the oceanic lithosphere at mid-oceanic ridges. (a) Schematic illustration of the serpentinization process at mid-oceanic ridges. Seawater percolates at depth through fractures in the footwall of detachment faults and enhanced the serpentinization of mantle peridotites (e.g. SWIR and Rainbow basement). The emplacement of hot and ductile metagabbros at shallow depth provides heat and potentially leads to a new serpentinization stage dominated by sulfur rich fluids at depth, near to mafic lithologies (e.g. MARK), or along hydrothermal fluid pathways (Rainbow stock work). At seafloor level, various studies (e.g. Schwarzenbach et al., 2012) have shown that microbial activity can drive sulfate reduction resulting in the formation of sulfide rich serpentinites. (b–d) Thin section sketches showing the evolution of serpentine textures and sulfur distribution at microscale. The progressive serpentinization of abyssal peridotites in seawater dominated system is accompanied with the disappearance of mantle phases, including sulfide oxidation (1), and the crystallization of sulfate-bearing serpentine (b–c). The recrystallization of serpentinites near H_2S-bearing hydrothermal field is accompanied with a decrease in sulfur concentrations in serpentines and the precipitation of abundant sulfides (d) suggesting a redistribution and reduction of sulfur (2). HT: High Temperature.

The high sulfur contents of serpentine minerals and the positive correlations between F, Cl and S (Fig. 6a,b) suggest that mantle sulfide oxidation cannot be the only source of sulfur in serpentinites, as sulfides do not contain significant F or Cl. Therefore, the F, Cl and S increase in serpentine must also be related to seawater circulation during the serpentinization process (Fig. 7c,d). This is in good agreement with previous studies that reported the formation of sulfate rich-serpentinites with $\delta^{34}S$ values close to that of seawater (Alt and Shanks, 1998, 2003; Delacour et al., 2008a, 2008b). This suggests that the sulfate contents in serpentine minerals could be originated from a mixture of seawater sulfate with sulfate derived from the oxidation of mantle sulfides initially present in the protolith.

The MARK and Rainbow stockwork serpentinites display lower $S^{6+}/\sum S$ relative to that of the SWIR or the Rainbow basement (Table 2, Fig. 3). In these rocks, serpentine display relatively low S-contents and are associated with disseminated micro-sulfides (Fig. 1b,c). The preferential partitioning of sulfur into sulfides seems to be related to the percolation of S-bearing fluids. In both settings, gabbroic intrusions provide heat and can drive high temperature hydrothermal systems (e.g., black smokers of the Rainbow massif). The percolation of seawater in metagabbros is accompanied with sulfide leaching and produces sulfur-rich fluids (Alt and Shanks, 2003; Fig. 7b). Considering that in hydrothermal fluids sulfur is mainly mobile as H_2S (e.g. Charlou et al., 2002), the percolation of such fluids in abyssal serpentinized peridotites may enhance the recrystallization of serpentine, the reduction of sulfate ($Fe–SO_4$ in equation (5) for simplicity) and the subsequent crystallization of sulfides (Fig. 7d), e.g.:

$$4H_2S + FeSO_4 \rightarrow FeS + 4H_2O \quad (5)$$

This scenario suggests an increase of S concentrations in bulk rock during H_2S fluid percolation which is in good agreement with the high sulfur concentrations of serpentinites formed in these settings (Alt and Shanks, 2003; Marques et al., 2007). It should be noted that crystallization of sulfide rich serpentinites is not necessarily restricted to abiotic settings. Previous studies have shown that the action of sulfate reducing bacteria can also occur in serpentinites altered at low-temperatures (<100 °C; Fig. 7e). In these contexts, serpentinites are also able to display high sulfide concentration (up to thousands of ppm; e.g. Schwarzenbach et al., 2012).

6. Conclusions

Our new μ-XANES analyses of serpentine textures show the presence of S^{6+} in the absence of sulfate bearing micro-phases (e.g. barite, anhydrite). Thus, our results indicate that sulfur can reside directly in the serpentine crystal structure in its oxidized form. In addition, in S^{6+}-rich samples, the homogeneous distribution of sulfur (Fig. 1a) and the correlations between sulfur and fluorine (or chlorine) concentrations (Fig. 6) in serpentine minerals are also suggestive of a structural incorporation of sulfur in serpentine, since classical sulfur-bearing minerals (e.g. pyrite, pyrrhotite, barite, anhydrite) are fluorine- (or chlorine-)free. Finally based on the strong similarity between haüyne and serpentine mineral spectra, we hypothesize that S has a similar short-distance atomic environment in both minerals (i.e. tetra-coordinated), and that it may be trapped as sulfate ions within the hexagonal vacancies of the tetrahedral (SiO_4) network.

Serpentinite bulk rock and in situ measurements of sulfur oxidation state and concentrations into serpentinites at mid-oceanic ridges show that in our samples the sulfur budget is mainly carried by sulfate-bearing serpentine minerals and/or the sulfides pyrite and pyrrhotite. Mixed lizardite and chrysotile assemblages can incorporate variable amounts of sulfur ranging from 140 to 1350 ppm. However, antigorite bearing assemblages display low sulfur concentrations (<100 ppm) in both oceanic or subduction settings. The incorporation of sulfate ions into serpentine minerals mainly occurs during the percolation of seawater-derived fluids through the lithosphere and the concomitant oxidation of mantle sulfides. This process can contribute to the production of H_2 observed at mid-oceanic ridges. In these settings a low amount of hydrothermal sulfides is expected. In the studied contexts, the formation of sulfide-bearing serpentinites appears to occur in the

presence of metagabbros into the lithosphere. In these settings, sulfide leaching from adjacent metagabbros prior to serpentinization leads to the formation of H_2S-rich fluids. The percolation of these fluids into sulfate-bearing serpentinites, near hydrothermal fields or at depth close to the metagabbros, leads to a decrease of sulfur content in serpentine minerals and the subsequent precipitation of sulfides.

Acknowledgements

We acknowledge SOLEIL for provision of synchrotron radiation facilities on LUCIA beamline (projects No. 20150534). Access to the Edinburgh Ion Microprobe Facility through Natural Environment Research Council (NERC) Scientific Services is gratefully acknowledged (project No. IMF517/0514). We warmly thank J. Craven (Edinburgh, UK) for his help, expertise, interest and support during samples preparation and SIMS analyses. We thank I. Daniel (LGL, Lyon) for fruitful discussions on serpentine structure. We thank J. Alt and an anonymous reviewer for critical comments on earlier version of this article, and careful editorial handling by T. Mather. This work was supported by a NERC Deep Volatiles Consortium Grant (NE/M000303/1) and an European Research Council Starting Grant (HabitablePlanet; 306655) awarded to H.W.

Appendix. Supplementary material

Supplementary material related to this article can be found online at http://dx.doi.org/10.1016/j.epsl.2017.02.029.

References

Agrinier, P., Cannat, M., 1997. Oxygen isotope constraints on serpentinization processes in ultramafic rocks from the Mid-Atlantic Ridge (23°N). Proc. Ocean Drill. Program Sci. Results 148, 381–388.

Alonso Mori, R., Paris, E., Giuli, G., Eeckhout, S.G., Kavcic, M., Zitnik, M., Bucar, K., Pettersson, L.G.M., Glatzel, P., 2009. Electronic structure of sulfur studied by X-ray absorption and emission spectroscopy. Anal. Chem. 81, 6516–6525.

Alt, J.C., Shanks, W.C., 1998. Sulfur in serpentinized oceanic peridotites: serpentinisation processes and microbial sulfate reduction. J. Geophys. Res. 103, 9917–9929.

Alt, J., Shanks, W.C., 2003. Serpentinization of abyssal peridotites from the MARK area, Mid Atlantic Ridge: sulfur geochemistry and reaction modeling. Geochim. Cosmochim. Acta 67, 641–653.

Alt, J.C., Shanks III, W.C., Bach, W., Paulick, H., Garrido, C.J., Beaudoin, G., 2007. Hydrothermal alteration and microbial sulfate reduction in peridotite and gabbro exposed by detachment faulting at the Mid-Atlantic Ridge, 15°20′N (ODP Leg 209): a sulfur and oxygen isotope study. Geochem. Geophys. Geosyst. 8, Q08002. http://dx.doi.org/10.1029/2007GC001617.

Alt, J.C., Garrido, C.J., Shanks, W.C., Turchyn, A., Padrón-Navarta, J.A., Sánchez-Vizcaíno, V.L., Pugnaire, M.T.G., Marchesi, C., 2012. Tracing the recycling of water, carbon, and sulfur during subduction metamorphism of seafloor serpentinites: a stable isotope study of the Almirez Massif, Spain. Earth Planet. Sci. Lett. 327–328, 50–60.

Alt, J., Schwarzenbach, E.M., Früh-Green, G.L., Shanks, W.C.S., Bernasconi, S.M., Garrido, C.J., Crispini, L., Gaggero, L., Padrón-Navarta, J.A., Marchesi, C., 2013. The role of serpentinites in cycling of carbon and sulfur: seafloor serpentinization and subduction metamorphism. Lithos 178, 40–54.

Andreani, M., Mével, C., Boullier, A.-M., Escartin, J., 2007. Dynamic control on serpentine crystallization in veins: constraints on hydration processes in oceanic peridotites. Geochem. Geophys. Geosyst. 8. http://dx.doi.org/10.1029/2006GC001373.

Andreani, M., Muñoz, M., Marcaillou, C., Delacour, A., 2013. μXANES study of iron redox state in serpentine during oceanic serpentinization. Lithos 178, 70–83.

Andreani, M., Escartin, J., Delacour, A., Ildefonse, B., Godard, M., Dyment, J., Fallick, A.E., Fouquet, Y., 2014. Tectonic structure, lithology, and hydrothermal signature of the Rainbow massif (Mid-Atlantic Ridge 36°14′N). Geochem. Geophys. Geosyst. 15. http://dx.doi.org/10.1002/2014GC005269.

Berndt, M.E., Allen, D.E., Seyfried, W.E., 1996. Reduction of CO_2 during serpentinization of olivine at 300 °C and 500 bar. Geology 24, 351–354.

Brearley, A.J., Barnes, J.D., Sharp, Z.D., 2007. Chrysotile nanotubes: potential host of insoluble chlorine in serpentinized oceanic crust. In: Abstracts of AGU Fall Meeting, #V11E-04.

Canales, J.P., Collins, J.A., Escartin, J., Detrick, R.S., 2000. Seismic structure across the rift valley of the Mid-Atlantic ridge at 23°20′N (MARK area): implications for crustal accretion processes at slow-spreading ridges. J. Geophys. Res. 105, 28411–28425.

Canfield, D.E., 2005. The early history of atmospheric oxygen: homage to Robert M. Garrels. Annu. Rev. Earth Planet. Sci. 33, 1–36.

Canil, D., O'Neil, H.St.C., Pearson, D.G., Rudnick, R.L., McDonough, W.F., Carswell, D.A., 1994. Ferric iron in peridotites and mantle oxidation state. Earth Planet. Sci. Lett. 123, 205–220.

Cannat, M., Fontaine, F., Escartín, 2010. Serpentinization and Associated Hydrogen and Methane Fluxes at Slow Spreading Ridges. Geophys. Monogr., vol. 188. American Geophysical Union, pp. 241–263.

Charlou, J., Donval, J.P., Fouquet, Y., Jean-Baptiste, P., Holm, N., 2002. Geochemistry of high H_2 and CH_4 vent fluids issuing from ultramafic rocks at the Rainbow hydrothermal field (36°14′N, MAR). Chem. Geol. 191, 345–359.

Debret, B., Nicollet, C., Andreani, M., Schwartz, S., Godard, M., 2013. Three steps of serpentinization in an eclogitized oceanic serpentinization front (Lanzo Massif – Western Alps). J. Metamorph. Geol. 31, 165–186.

Debret, B., Koga, K., Nicollet, C., Andreani, M., Schwartz, S., 2014a. F, Cl and S input via serpentinite in subduction zones: implications on the nature of the fluid released at depth. Terra Nova 26, 96–101.

Debret, B., Andreani, M., Muñoz, M., Bolfan-Casanova, N., Carlut, J., Nicollet, C., Schwartz, S., Trcera, N., 2014b. Evolution of Fe redox state in serpentine during subduction. Earth Planet. Sci. Lett. 400, 206–218.

Debret, B., Millet, M.-A., Pons, M.-L., Bouilhol, P., Inglis, E., Williams, H., 2016. Isotopic evidence for iron mobility during subduction. Geology 44, 215–218.

Deer, W., Howie, R.A., Zussman, J., 2012. Introduction to the Rock-Forming Minerals, 3rd edition. Mineralogical Society of Great Britain and Ireland.

Delacour, A., Früh-Green, G.L., Bernasconi, S.M., Kelley, D.S., 2008a. Sulfur in peridotites and gabbros at Lost City (30°N, MAR): implications for hydrothermal alteration and microbial activity during serpentinization. Geochim. Cosmochim. Acta 72, 5090–5110.

Delacour, A., Früh-Green, G.L., Bernasconi, S.M., 2008b. Sulfur mineralogy and geochemistry of serpentinites and gabbros of the Atlantis Massif (IODP Site U1309). Geochim. Cosmochim. Acta 72, 5111–5127.

Evans, K.A., 2012. The redox budget of subduction zones. Earth-Sci. Rev. 113, 11–32.

Feuillie, C., Daniel, I., Michot, L.J., Pedreira-Segade, U., 2013. Adsorption of nucleotides onto Fe–Mg–Al rich swelling clays. Geochim. Cosmochim. Acta 120, 97–108.

Fleet, M.E., 2005. XANES spectroscopy of sulfur in Earth materials. Can. Mineral. 43, 1811–1838.

Frost, B.R., 1985. On the stability of sulfides, oxides and native metals in serpentinite. J. Petrol. 26, 31–63.

Hattori, K.H., Guillot, S., 2007. Geochemical character of serpentinites associated with high- to ultrahigh-pressure metamorphic rocks in the Alps, Cuba, and the Himalayas: recycling of elements in subduction zones. Geochem. Geophys. Geosyst. 8, Q09010. http://dx.doi.org/10.1029/2007GC001594.

Hattori, K., Takahashi, Y., Guillot, S., Johanson, B., 2005. Occurrence of arsenic (V) in forearc mantle serpentinites based on X-ray absorption spectroscopy study. Geochim. Cosmochim. Acta 69, 5585–5596.

Jugo, P.J., Wilke, M., Botcharnikov, R.E., 2010. Sulfur K-edge XANES analysis of natural and synthetic basaltic glasses: implications for S speciation and S content as function of oxygen fugacity. Geochim. Cosmochim. Acta 74, 5926–5938.

Klein, F., Bach, W., 2009. Fe–Ni–Co–O–S phase relations in peridotite seawater interactions. J. Petrol. 50, 37–59.

Klimm, K., Kohn, S.C., O'Dell, L.A., Botcharnikov, R.E., Smith, M.E., 2012. The dissolution mechanism of sulphur in hydrous silicate melts. I: assessment of analytical techniques in determining the sulphur speciation in iron-free to iron-poor glasses. Chem. Geol. 322, 237–249.

Lafay, R., Montes-Hernandez, G., Janots, E., Munoz, M., Auzende, A.L., Gehin, A., Chiriac, R., Proux, O., 2016. Experimental investigation of As, Sb and Cs behavior during olivine serpentinization in hydrothermal alkaline systems. Geochim. Cosmochim. Acta 179, 177–202.

Marques, A.F.A., Barriga, F.J.A.S., Scott, S.D., 2007. Sulfide mineralization in an ultramafic-rock hosted seafloor hydrothermal system: from serpentinization to the formation of Cu–Zn–(Co)-rich massive sulfides. Mar. Geol. 245, 20–39.

Mellini, M., 2005. Micro- and mesoporous carbon forms, chrysotile, and clathrates. In: Ferraris, G., Merlino, S. (Eds.), Micro- and Mesoporous Mineral Phases. Rev. Mineral. Geochem. 57, 435–448.

Métrich, N., Bonnin-Mosbah, M., Susini, J., Menez, B., Galoisy, L., 2002. Presence of sulfite (S-IV) in arc magmas: implications for volcanic sulfur emissions. Geophys. Res. Lett. 29, 4.

Métrich, N., Berry, A.J., O'Neill, H.S.C., Susini, J., 2009. The oxidation state of sulfur in synthetic and natural glasses determined by X-ray absorption spectroscopy. Geochim. Cosmochim. Acta 73, 2382–2399.

Orberger, B., Metrich, N., Mosbah, M., Mevel, C., Fouquet, Y., 1999. Nuclear microprobe analysis of serpentine from the mid-Atlantic ridge. Nucl. Instrum. Methods Phys. Res. B 158, 575–581.

Pabst, S., Zack, T., Savov, I.P., Ludwig, T., Rost, D., Vicenzi, E.P., 2011. Evidence for boron incorporation into the serpentine crystal structure. Am. Mineral. 96, 1112–1119.

Ravel, B., Newville, M., 2005. ATHENA, ARTEMIS, HEPHAESTUS: data analysis for X-ray absorption spectroscopy using IFEFFIT. J. Synchrotron Radiat. 12, 537–541.
Reynard, B., 2013. Serpentine in active subduction zones. Lithos 178, 171–185.
Rouméjon, S., Cannat, M., 2014. Serpentinization of mantle-derived peridotites at mid-ocean ridges: mesh texture development in the context of tectonic exhumation. Geochem. Geophys. Geosyst. 15, 2354–2379.
Rouméjon, S., Cannat, M., Agrinier, P., Godard, M., Andreani, M., 2015. Serpentinization and fluid pathways in tectonically exhumed peridotites from the Southwest Indian Ridge (62–65E). J. Petrol. 56, 703–734.
Sauter, D., Cannat, M., Roumejon, S., Andreani, M., Birot, D., Bronner, A., Brunelli, D., Carlut, J., Delacour, A., Guyader, V., MacLeod, C.J., Manatschal, G., Mendel, V., Menez, B., Pasini, V., Ruellan, E., Searle, R., 2013. Continuous exhumation of mantle-derived rocks at the Southwest Indian Ridge for 11 million years. Nat. Geosci. 6, 314–320.
Schwarzenbach, E., Früh-Green, G.L., Bernasconi, S.M., Alt, J.C., Shanks, W.C., Gaggero, L., Crispini, L., 2012. Sulfur geochemistry of peridotite-hosted hydrothermal systems: comparing the Ligurian ophiolites with oceanic serpentinites. Geochim. Cosmochim. Acta 91, 283–305.
Van den Bleeken, G., Koga, K.T., 2015. Experimentally determined distribution of fluorine and chlorine upon hydrous slab melting, and implications for F–Cl cycling through subduction zones. Geochim. Cosmochim. Acta 171, 353–373.
Wilke, M., Jugo, P.J., Klimm, K., Susini, J., Botcharnikov, R., Kohn, S.C., Janousch, M., 2008. The origin of S^{4+} detected in silicate glasses by XANES. Am. Mineral. 93, 235–240.
Wilke, M., Klimm, K., Kohn, S.C., 2011. Spectroscopic studies on sulfur in synthetic and natural glass. In: Behrens, H., Webster, J.D. (Eds.), Sulfur in Magmas and Melts and Its Importance for Natural and Technical Processes. In: Rev. Mineral. Geochem., vol. 73, pp. 41–78.
Wunder, B., Deschamps, F., Watenphul, A., Guillot, S., Meixner, A., Romer, R.L., Wirth, R., 2010. The effect of chrysotile-nanotubes on the serpentine-fluid Li-isotopic fractionation. Contrib. Mineral. Petrol. 159, 781–790.